PASJ: Publ. Astron. Soc. Japan , 1–??,
© 2016. Astronomical Society of Japan.

arXiv:1603.00202v1 [astro-ph.HE] 1 Mar 2016

Peculiar Lapse of Periodic Eclipsing Event at Low Mass X-ray Binary GRS 1747−312 during Suzaku Observation in 2009

Shigetaka Saji,[1] Hideyuki Mori,[2,3] Hironori Matsumoto,[4] Tadayasu Dotani,[5, 6, 7] Masachika Iwai,[6, 5]
Yoshitomo Maeda,[5, 7] Ikuyuki Mitsuishi, [1] Masanobu Ozaki,[5] Yuzuru Tawara, [1]
[1]*Division of Particle and Astrophysical Science, Graduate School of Science, Nagoya University, Furo-cho, Chikusa-ku, Nagoya, 464-8602*
[2]*CRESST and X-ray Astrophysics Laboratory, Code 602, NASA/Goddard Space Flight Center, Greenbelt, MD 20771, USA*
[3]*Department of Physics, University of Maryland, Baltimore County, 1000 Hilltop Circle, Baltimore, MD 21250, USA*
[4]*Kobayashi-Maskawa Institute for the Origin of Particles and the Universe, Nagoya University, Furo-cho, Chikusa-ku, Nagoya, 464-8602*
[5] *Institute of Space and Astronautical Science (ISAS), Japan Aerospace Exploration Agency (JAXA), 3-1-1, Yoshinodai, Chuo-ku, Sagamihara, 252-5210*
[6]*Tokyo Institute of Technology, 121, Ookayama 2chome, Meguro-ku, Tokyo, 1528550, Japan*
[7]*Department of Space and Astronautical Science, SOKENDAI (The Graduate University for Advanced Studies), 3-1-1 Yoshinodai, Chuo-ku, Sagamihara, Kanagawa 252-5210, Japan*
s_saji@u.phys.nagoya-u.ac.jp

(Received ; accepted)

Abstract

GRS 1747−312 is a neutron star Low-Mass X-ray Binary in the globular cluster Terzan 6, located at a distance of 9.5 kpc from the Earth. During its outbursts, periodic eclipses were known to occur. Observations for the outbursts were performed with Chandra in 2004 and Swift in 2013. XMM-Newton observed its quiescent state in 2004. In addition, when Suzaku observed it in 2009 as a part of Galactic center mapping observations, GRS 1747−312 was found to be in a low luminosity state with $L_{\rm x} \sim 1.2 \times 10^{35}$ erg s^{-1}. All of the observations except for XMM-Newton included the time of the eclipses predicted. We analyzed archival data of these observations. During the Chandra and Swift observations, we found clear flux decreases at the expected time of the eclipses. During the Suzaku observation, however, there were no clear signs for the predicted eclipses. The lapse of the predicted eclipses during the Suzaku observation can be explained by a contaminant source quite close to GRS 1747−312. When GRS 1747−312 is in the quiescent state, we observe X-rays from the contaminant source rather than from GRS 1747−312. However, we have no clear evidence for the contaminant source in our data. The lapse might also be explained by thick material ($N_{\rm H} > 10^{24}$ cm^{-2}) between the neutron star and the companion star, though the origin of the thick material is not clear.

Key words: X-rays: binaries$_1$ — X-rays: individuals (GRS 1747−312)$_2$ — stars: neutron$_3$ — binaries: eclipsing$_4$

1. Introduction

Low Mass X-ray Binaries (LMXBs) are stellar systems consisting of a compact object and a low-mass ($\lesssim 1 M_\odot$) companion star. The companion star supplies gas onto the compact star by Roche-lobe overflow. The accreting matter releases the gravitational energy and then emits X-rays. Many LMXBs exhibit large variability in X-ray luminosity between $10^{32} - 10^{33}$ erg s^{-1} (quiescent state) and $10^{37} - 10^{38}$ erg s^{-1} (outburst state). So far, more than 100 LMXBs have been identified in the Galaxy (Liu et al. 2007). Among them, only six are known to have clear X-ray eclipses: EXO 0748−676 (Wolff et al. 2009), XTE J1710−281 (Jain & Paul 2011), X 1658−298 (Oosterbroek et al. 2001), AX J1745.6−2910 (Maeda et al. 1996; Kennea & Skinner 1996), 4U 2129+47 (Lin et al. 2009) and GRS 1747−312 (this work). An eclipsing feature informs us of an accurate orbital period and a strong limitation on an inclination angle of the system.

GRS 1747−312 is a transient X-ray source firstly detected in 1990 with ROSAT (Predehl et al. 1991) and Granat (Pavlinsky et al. 1994). The source is located at $(\alpha, \delta)_{\rm J2000.0} = (267.^\circ69526, -31.^\circ27468)$ or $(l, b) = (358.^\circ57274, -2.^\circ16286)$. The position was determined with the Chandra HRC-I with an uncertainty of $0.''4$ (in't Zand et al. 2003). The position is coincident with Terzan 6, which is a core-collapsed metal-rich globular cluster (Barbuy et al. 1997). The distance to the cluster is estimated to be $9.5^{+3.3}_{-2.5}$ kpc from the luminosity level of the horizontal branch (Kuulkers et al. 2003). The compact object in GRS 1747−312 is considered to be a neutron star, since four type-I X-ray bursts from GRS 1747−312 were detected (in't Zand et al. 2003). Assuming the distance for Terzan 6, the peak flux of the type-I bursts was consistent with the flux of a neutron star at the Eddington luminosity. Thus GRS 1747−312 is thought to belong to

the cluster. In the HRC-I observation, no other X-ray sources were detected in the cluster. The detection limit of the observation was 1.3×10^{-13} erg cm^{-2} s^{-1} (in't Zand et al. 2003).

It is known that GRS 1747−312 exhibits recurrent X-ray outbursts with an interval of about 130–142 days (in't Zand et al. 2003). Typical time scale of the decay of the outbursts was ~ 18 days. During the outburst, BeppoSAX and Rossi X-ray Timing Explorer (RXTE) observations found periodic eclipses with a duration of 2596 s. The authors claimed that the orbital period is $P = 0.514980303$ days. The duration of the eclipse and the orbital period indicate that the mass of the companion star is at least 0.1 $M_\odot$ assuming a mass of 1.4 $M_\odot$ for the neutron star. Based on the typical age of a globular cluster, the mass of the companion star is thought to be lower than 0.8 $M_\odot$ (in't Zand et al. 2000).

An energy spectrum of GRS 1747−312 during the outburst obtained with BeppoSAX was investigated in in't Zand et al. (2000). No line-like structures were detected in the energy range between 1 keV and 100 keV. The spectrum was represented well by a two-component model consisting of a blackbody and a Comptonized emission; the blackbody temperature was $kT = 1.78$ keV, while the Comptonized component has an electron temperature of $kT_e = 5.4$ keV, an optical depth of $\tau = 7.4$, and a temperature of seed emission of $kT_{seed} = 0.57$ keV. The spectral analysis demonstrated that the absorption column density was approximately 10^{22} cm^{-2}, which is consistent with the value obtained from the interstellar reddening of Terzan 6 (in't Zand et al. 2000; Predehl & Schmitt 1995).

Previous studies of GRS 1747−312, however, were concentrated on the outburst state. Thus the behavior outside the outbursts is still unclear. In this paper, we analyzed archival data of Chandra, XMM-Newton, Suzaku and Swift to investigate physical properties in various states. Detailed information on the observations is described in section 2. Results on imaging, timing and spectral analysis are reported in section 3. Discussions and conclusions are given in sections 4 and 5, respectively. In this paper, the uncertainties are at the 90% confidence level, while the errors on the data points of spectra, radial profiles, and light curves are at the 1σ level, unless otherwise stated.

2. Observation and data reduction

2.1. Chandra

Chandra (Weisskopf et al. 2000) has an X-ray telescope named High Resolution Mirror Assembly with an angular resolution of $0\farcs5$. The telescope focuses X-rays onto one of two kinds of instruments, Advanced CCD Imaging Spectrometer (ACIS; Garmire et al. 2003) or High Resolution Camera (HRC; Murray et al. 2000). Chandra is equipped with two grating spectrometers, High Energy Transmission Grating (HETG; Canizares et al. 2005) and Low Energy Transmission Grating (LETG; Brinkman et al. 2000); the HETG covers the energy range of 0.4–10 keV and the LETG covers 0.07–0.2 keV.

GRS 1747−312 was observed twice with Chandra on 2000 March 9 (ObsID = 720) and on 2004 March 29 (ObsID = 4551). The observation in 2000 was published by in't Zand et al. (2003) to determine the source position with the HRC. Thus, we focus on the data obtained from the observation in 2004 hereafter. The observation was conducted as a Target of Opportunity (ToO) to obtain the data during the outburst, and it covered the time of the eclipse (see section 3.2). The log of the observation is summarized in table 1.

The observation was operated with the ACIS-S in the Continuous Clocking (CC) mode. The ACIS-S contains six X-ray CCD chips arranged in a 1×6 array, and each chip has 1024×1024 pixels. The field of view is $8\farcm3 \times 50\farcm6$. In the CC mode, two-dimensional images cannot be obtained, but a high time resolution of 2.85 ms can be achieved. An energy resolution is 95 eV at 1.49 keV and 150 eV at 5.9 keV. During the observation, the HETG was inserted between the telescope and the ACIS-S. We only used the zeroth order image for our analysis.

We analyzed the primary event data processed with `Standard Data Processing pipeline Version DS 8.4` with a software package `CIAO version 4.6` and a relevant calibration database (`CALDB version 4.6.1.1`).

2.2. XMM-Newton

GRS 1747−312 (a.k.a. 1RXS J175046.5−311632) was observed with XMM-Newton in 2004 September 28. XMM-Newton (Jansen et al. 2001) enables us to conduct imaging spectroscopy in the 0.3–10 keV band, utilizing the X-ray telescopes (Aschenbach et al. 2000) and the focal plane detectors called European Photon Imaging Camera (EPIC). EPIC consists of two types of X-ray CCDs: Metal Oxide Semiconductor (MOS) CCDs (Turner et al. 2001) and pn CCDs (Strüder et al. 2001). There are two MOS detectors (MOS1 and MOS2). The EPIC cameras were operated with the medium filter in the full-frame mode in this observation. The total exposure time were 8.2 ks for pn and 14.3 ks for each MOS detector.

We reprocessed the Observation Data Files provided by the XMM-Newton Science Archive with `epchain` and `emchain`, using appropriate calibration data. We then used the Science Analysis Software (`SAS, version 13.0`) to make images, light curves and spectra. In order to excise flaring particle backgrounds mainly caused by particles such as soft protons, we filtered out the reprocessed event files, following the instruction in the XMM data reduction guide[1]. We made X-ray light curves of single events (`PATTERN` = 0) in the 10–12 keV band for pn and above 10 keV for MOS1/2. The events were accumulated from the entire field of view of each detector. The good time intervals were selected so that the count rates are smaller than 0.4 cts s^{-1} for pn or 0.35 cts s^{-1} for MOS1/2. We found that the observation was little affected by the background flares: the screened live times for pn and MOS1/2 were 8.2 ks and 14.2 ks, respectively.

[1] http://xmm-tools.cosmos.esa.int/external/xmm_user_support/documentation/sas_usg/USG.pdf

In the following analysis, we used the screened event data. The observation log is summarized in table 1.

2.3. Suzaku

GRS 1747−312 was also observed with Suzaku (Mitsuda et al. 2007) in 2009 September 16. The observation was performed as a part of the mapping observation of the Galactic center region. The information on the Suzaku observation is also given in table 1.

One of the main instruments of Suzaku is the X-ray Imaging Spectrometer (XIS) consists of four sets of CCD cameras (XIS0-3) (Koyama et al. 2007). Each CCD chip is placed on the focal plane of the X-Ray Telescope (XRT; Serlemitsos et al. 2007). XIS0, 2 and 3 are front-illuminated (FI) CCDs, while XIS1 is a back-illuminated (BI) CCD. Since XIS2 suffered serious damage, it has not been usable since 2006 November 9. In this observation, the XIS was operated in the normal clocking mode with the Spaced-row Charge Injection (SCI; Uchiyama et al. 2009). Suzaku also has the Hard X-ray Detector (HXD ; Takahashi et al. 2007). The HXD consists of Si-PIN photo diodes and GSO scintillators. Although the HXD is a non-imaging detector, the PIN and GSO provide us X-ray spectra covering the energy ranges of 10–70 keV and 40–600 keV, respectively. The HXD was operated in the normal mode in this observation.

We analyzed the cleaned event data processed with the `processing version of 2.4.12.27`. In this process, the data taken at the South Atlantic Anomaly (SAA) and low elevation angles of < 5 deg from the night-earth rim and < 20 deg from the day-earth rim were excluded. The net exposure time was 45.3 ks for the XIS and 45.6 ks for the HXD. To analyze the data, we used the software package `HEAsoft version 6.12`, and the relevant calibration database (`CALDB`). We generated the redistribution matrix files (RMFs) and ancillary response files (ARFs) by `xisrmfgen` and `xissimarfgen` (Ishisaki et al. 2007).

2.4. Swift

On 2013 March 11, INTEGRAL/JEM-X (Lund et al. 2003) detected a burst from GRS 1747−312 (Chenevez et al. 2013). Soon after the detection, Monitor of All-sky X-ray Image (MAXI; Matsuoka et al. 2009) on board the International Space Station (ISS) gave a transient alert on March 11[2]. Subsequently, two ToO observations were performed with Swift on March 18 and March 24. The exposure for each observation was ~ 1 ks. The 2nd observation was planned to observe the predicted ingress of the eclipse.

We used Swift X-Ray Telescope (XRT) data of these observations. Swift XRT (Gehrels et al. 2004) consists of an X-ray telescope and a single X-ray CCD (600×602 pixel), which covers the 0.2–10 keV energy band. The CCD has the same design with that of the EPIC MOS instruments of XMM-Newton. The size of the field of view is $23\farcm6 \times 23\farcm6$. In these observations, the XRT was operated with the Photon Counting (PC) mode. The observation logs are also summarized in table 1.

We analyzed the cleaned event data which were generated by the Swift Data Center (SDC) processing. We used the `HEAsoft version 6.16` to analyze the Swift XRT data. Also, we used a relevant calibration database (`CALDB Version 1.8`).

[2] http://maxi.riken.jp/pipermail/x-ray-star/2013-March/000210.html

3. Analysis and results

3.1. Image

Although only GRS 1747−312 were detected in Terzan 6 during the HRC observation, there may be other transient X-ray sources in the cluster because of the high number density of the stellar objects. Thus, in this section, we analyzed X-ray images of the observations to investigate whether only GRS 1747−312 is visible or not. Then we defined source and background regions for the following light curve and spectral analyses.

3.1.1. Chandra

Since the ACIS was operated in the CC mode, only a one-dimensional image which is parallel to the long axis of the ACIS-S can be obtained. A peak of the brightness was seen near the center of the image. Since the image rotated only by $2\fdg4$ clockwise from the north direction, we can study the position of the peak only along the declination axis. A count profile along the declination axis in the 0.5–10 keV band binned with $0\farcs28$ is shown in figure 1. The origin of the horizontal axis is set to the position of GRS 1747−312, $Dec. = -31\fdg27468$, given by the Chandra HRC observation (in't Zand et al. 2003). We fitted the profile between $\pm 1''$ with a Gaussian function and found that the peak position is $\delta Dec. = +0\farcs208 \pm 0\farcs001$. Since the 90% uncertainty circle of the Chandra X-ray absolute position has a radius of $0\farcs6$ (Weisskopf et al. 2003), the peak position is consistent with the position of GRS 1747−312. The width of the Gaussian function was $\sigma = 0\farcs353 \pm 0\farcs001$. We simulated a profile of a point source with `MARX` (Davis et al. 2012). The width of a Gaussian function fitted to the simulated profile was $\sigma = 0\farcs358$. A possibility of a spatially extended source or multiple objects is thus rejected. Though we could not study the image along the right ascension axis, the observed source seems consistent with GRS 1747−312.

In the following analysis, we extracted source photons from $-5''$ to $+5''$ in the profile (see figure 1). Also, background events were extracted from regions between $-25''$ and $-15''$ and between $+15''$ and $+25''$.

3.1.2. XMM-Newton

Figure 2 shows an X-ray image in the 0.5–10 keV band obtained with the XMM-Newton pn. The image was smoothed with a Gaussian function of $\sigma = 2$ pixels.

We found several sources in all pn, MOS1, and MOS2 images. Seven sources used later for the astrometry of the Suzaku image are indicated with green circles in figure 2. We designated them as Sources 1–7 hereafter. These sources were tagged as point sources by the source detection tool in the `SAS`, `emldetect`. Their positions are listed in table 2. The statistical error on the Source 1 posi-

Table 1. Summary of the observations for GRS 1747−312

Observatory	Obs.ID	Start time (UTC)	Exposure (ks)*	Outburst†	Eclipse‡
Chandra	4551	2004/03/29 22:53:48	45.0(ACIS-S/HETG)	√	√
XMM-Newton	206990101	2004/09/28 13:18:58	14.2 (MOS1/2), 8.2 (pn)		
Suzaku	504092010	2009/09/16 07:21:35	45.3 (XIS), 45.6 (PIN)		√
Swift	00032761001	2013/03/18 21:01:13	0.98(XRT)	√	
Swift	00032761002	2013/03/24 02:13:18	0.98(XRT)	√	√

* Effective exposure of the screened data; the HXD-PIN exposure is dead-time corrected.
† Observation during the outbursts.
‡ Observation including the predicted time of eclipses.

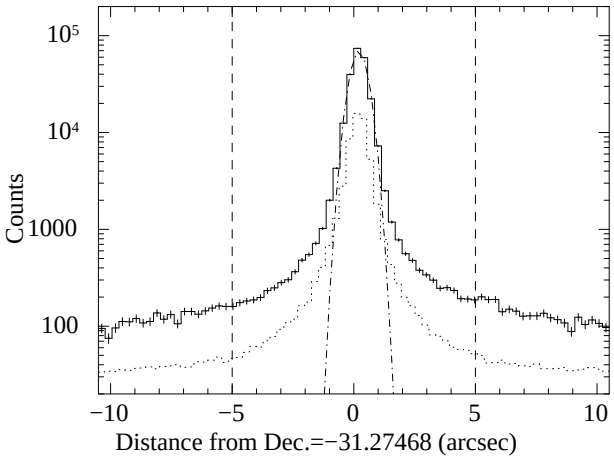

Fig. 1. Projection profile along the declination axis obtained with the Chandra ACIS-S in the 0.5–10 keV band. The bin size is 0.″28. The dash-dotted line shows the Gaussian function fitted to the profile between ±1″. The dotted line shows the profile simulated with `MARX`. To represent the background, a constant component is added. The normalization of the simulated profile is arbitrarily changed for the clarity. The region between the two dashed lines was defined as a source region.

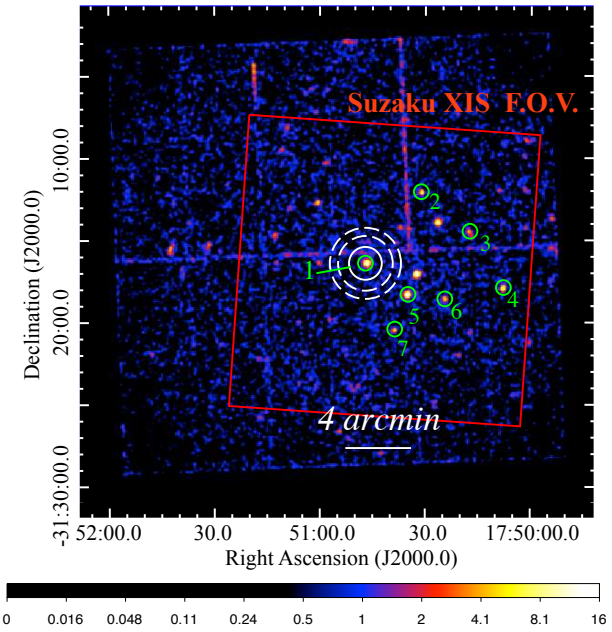

Fig. 2. XMM-Newton pn image in the 0.5–10 keV band smoothed with a Gaussian function of $\sigma = 2$ pixels. The solid circle and dashed annulus indicate the source and background regions. The green circles show the sources listed in table 2, which are used for the astrometry of the Suzaku image described in section 3.1.3. The red square corresponds to the field of view of the Suzaku XIS (see section 3.1.3).

tion is 0.″7, and Source 1 is coincident with GRS 1747−312 within an attitude uncertainty of XMM-Newton (3–4″)[3]. Source 1 can thus be regarded as GRS 1747−312.

We defined a source region as a circle with a radius of 60″ centered on GRS 1747−312. The source region is shown as the white solid circle in figure 2. A background region was defined as its surrounding annulus with inner and outer radii of 100″ and 130″. The center of the annulus is the same as that of the circle of the source region.

3.1.3. Suzaku

X-ray images in the 0.5–10 keV band were obtained with XIS0, 1, and 3. Since an X-ray source at the center of the images exhibited a burst and a dip-like behavior in the X-ray light curve as described in section 3.2, we excluded the durations of the burst and dip to create the XIS images. The images of XIS0, 1, and 3 were combined, and binned with 8×8 pixels.

All seven sources in table 2 can be seen in the Suzaku image. We then checked the astrometry between the Suzaku and XMM-Newton observations using these sources. We made projection profiles of these sources along the right ascension and declination axes from the Suzaku image. These profiles were fitted with a Gaussian function plus a constant component to determine the peak positions. Since Sources 4 and 5 were too faint to fit with the Gaussian function, we defined the pixel position having the largest count as the position of these sources. We found that the Suzaku positions were shifted on average by −1.″1 along the right ascension axis and by +10.″0 along the declination axis. We then corrected the coordinates of the Suzaku image by these amounts. The Suzaku image thus obtained is shown in figure 3, and the source positions are listed in table 2.

The Suzaku position of Source 1 is coincident with GRS 1747−312 within the Suzaku attitude uncertainty of ∼ 19” (Uchiyama et al. 2008). The radial profile of Source 1 was fitted with a point spread function extracted from the Suzaku data of SS Cyg. The profile is consistent

[3] XMM Users' Handbook: http://www.mssl.ucl.ac.uk/www_xmm/ukos/onlines/uhb/XMM_UHB/node104.html

Table 2. List of sources detected with XMM-Newton and Suzaku.

	XMM-Newton image		Suzaku XIS image		pn count rate
Number*	RA	Dec	RA	Dec	(cts s^{-1})
1	267.°6950	−31.°2750	267.°697	−31.°276	3.6 ± 0.3
2	267.°6301	−31.°2033	267.°630	−31.°205	1.6 ± 0.2
3	267.°5733	−31.°2435	267.°572	−31.°244	1.1 ± 0.2
4	267.°5335	−31.°3004	267.°535	−31.°301	2.7 ± 0.3
5	267.°6468	−31.°3071	267.°646	−31.°308	3.7 ± 0.3
6	267.°6026	−31.°3114	267.°603	−31.°311	1.2 ± 0.2
7	267.°6625	−31.°3430	267.°661	−31.°339	0.9 ± 0.2

* The numbers correspond to the ones in figures 2 and 3.

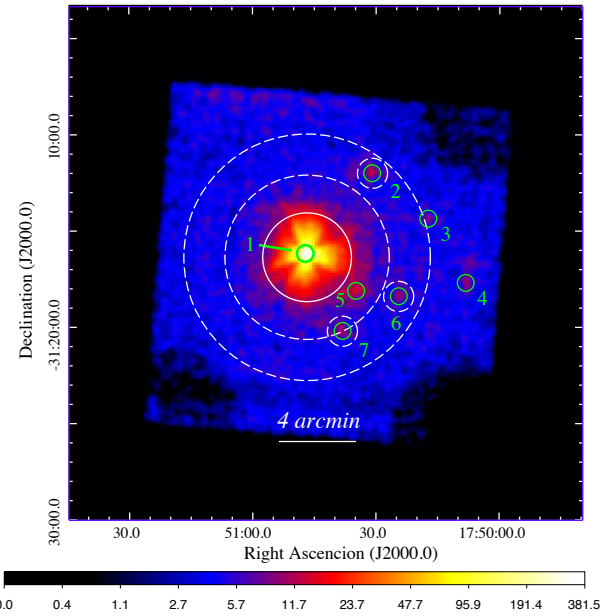

Fig. 3. Combined image of three XIS sensors in the 0.5–10 keV band after the coordinate correction as described in the text. X-ray events during the burst and dip were not used. Regions illuminated by the ^{55}Fe calibration sources were removed. The image was binned with 8×8 pixels and then smoothed with a Gaussian function of $\sigma = 2$ bins. The color bar at the bottom of the image is in unit of photons per binned pixel. The solid circle and the dashed annulus indicate the source and background regions. Green circles shows the sources listed in table 2.

with the point spread function with $\chi^2/\nu = 1.12$ ($\nu = 294$), where ν represents the degree of freedom in the fitting. Thus Source 1 can be regarded as GRS 1747−312.

Source 5 was located $\sim 3'$ away from GRS 1747−312 in the south-west direction, and we defined a source region as a circle with a radius of 2.′3 centered on GRS 1747−312 to avoid the contamination from source 5. The background events were extracted from an annulus with inner and outer radii of 4.′27 and 6.′45. Since Sources 2, 6 and 7 were located in the background region, we excluded X-ray photons within circles with a radius of 0.′78, centered on these sources. These regions are plotted as dashed circles in figure 3.

3.1.4. Swift

Figures 4a and 4b show X-ray images in the 0.5–10 keV band obtained with the Swift XRT during the 1st and 2nd observations, respectively. The images were binned with 2×2 pixels. Since there was a sudden decrease in the flux during the 2nd observation (see section 3.2.4), we filtered out the interval of the low-flux state to improve the signal-to-noise ratio. In both images, the brightness peak was located near the center of the field of view.

To determine the position of the X-ray source, we made projection profiles along the right ascension and declination axes, and then fitted the profiles with a Gaussian function. The projection profile of the 1st observation along the declination axis obtained from the green rectangular region in figure 4a is shown in figure 5. The profile within $\pm 10''$ looks suppressed. The suppression was also seen in the 2nd observation. This is because of the pile-up effect, since the X-ray source was too bright (> 2 cts s^{-1}). Although the profiles were not fully reproduced with a simple Gaussian function, the Gaussian fittings gave the source position as $(RA, Dec)_{\rm J2000.0} = (267.°6964, -31.°2741)$ for the 1st observation and (267.°6955, −31.°2748) for the 2nd observation. These values are coincident with the position of GRS 1747−312 within the fitting error ($\sim 1''$) and positional uncertainties of Swift ($\sim 3''$)[4]. Hence, we consider the X-ray source detected with the Swift XRT as GRS 1747−312.

We found an X-ray source at almost the same position as GRS 1747−312 even during the low-flux state in the 2nd observation. However, the statistics were too poor to do the above analysis. The pixel position with the maximum counts was $(RA, Dec)_{\rm J2000.0} = (267.°6925, -31.°2767)$. There was no significant change of the position from that during the high-flux state.

For the light curves and spectral analyses described in the following sections, we defined a source region as an annulus with an outer radius of 1.′5 centered on the position of GRS 1747−312. A circular region with a radius of $10''$ was excluded from the source region to remove the pileup events. A background region was defined as an annulus with inner and outer radii of 1.′5 and 3.′0. The center of the annulus was the same as that of the source

[4] Documentation for Swift XRT GRB positions: http://www.swift.ac.uk/sper/docs.php

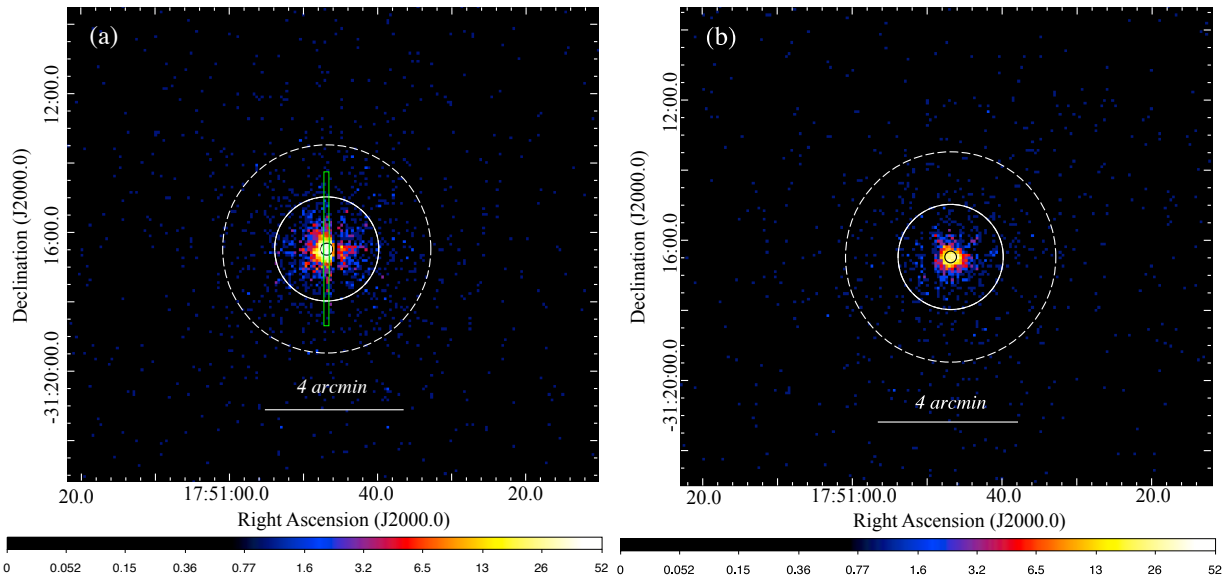

Fig. 4. Swift XRT images obtained during the 1st (a) and 2nd (b) observations in the 0.5–10 keV band. The region around GRS 1747−312 were zoomed up. The images were binned with 2×2 pixels. White solid and dashed circles show the source and background regions, respectively. We made the projection profile shown in figure 5 from the green rectangle. The black circles show the regions in which events were removed from the source regions to mitigate the pile-up effect.

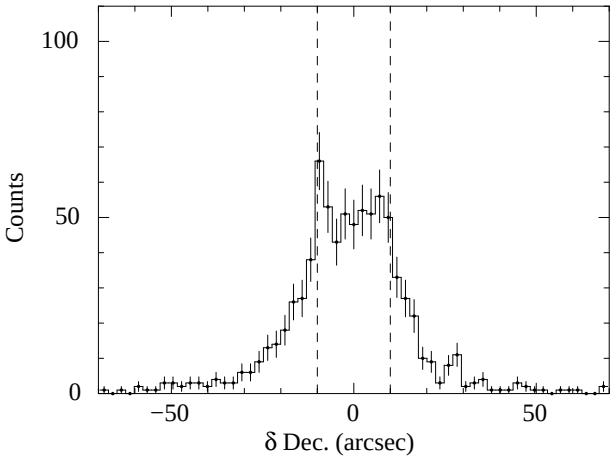

Fig. 5. Projection profile during the Swift 1st observation extracted from the green rectangular in figure 4 (a). The origin of the horizontal axis was set to be the position of GRS 1747−312. The bin size was 1 pixel (2.″36). X-ray events between the dashed lines were affected by the pileup, and they were not used in the following light curve and spectral analysis.

region. We made ARFs using `xrtmkarf` in `FTOOLS`, taking into account the bad columns at DETX = 290–294 and 319–321 [5] in the detector coordinate.

3.2. *Light curve*

3.2.1. *Chandra*

We extracted light curves in the 0.5–10 keV band from the source and background regions defined in section 3.1.1. The background light curve was subtracted from the source light curve after normalizing the difference of the area. Figure 6 shows the background-subtracted light curve binned with 46 s. The light curve is plotted in Terrestrial Time corrected to solar system barycenter (Barycentric Dynamical Time; TDB). The origin of the light curve is MJD 53093.96450. In the light curve, a sudden decline in the count rate from 17 ks to 19.5 ks and a burst at 43 ks were seen. The folding time of the exponential decay of the burst was $9.4^{+2.8}_{-2.2}$ s. The decay time scale is consistent with that of a typical type-I X-ray burst.

In in't Zand et al. (2003), the ephemeris of GRS 1747−312 was calculated as MJD 52066.259473(5) + 0.514980303(7)n for ingress and MJD 52066.289497(10) + 0.514980303(7)n for egress (n is an integer). Based on the ephemeris, the ingress and egress of eclipse were predicted at MJD 53094.16016 and 53094.19020 during the Chandra observation, respectively, which are shown with the dashed lines in figure 6. Both of the observed ingress and egress were coincident with the predicted time within ~ 10 s. Averaged count rates outside and during the eclipse were 5.43 ± 0.02 cts s^{-1} and 0.05 ± 0.01 cts s^{-1}, respectively. In this estimation, time intervals of 30 s before and after the ingress and egress were neglected to exclude the transition phases.

3.2.2. *XMM-Newton*

We made light curves of the pn, MOS1 and 2 from the source and background regions in the 0.5–10 keV band. In the background-subtracted light curves, no clear variability was seen. The averaged count rate was 0.029 ± 0.003 cts s^{-1} for pn and 0.027 ± 0.002 cts s^{-1} for MOS 1 + 2.

3.2.3. *Suzaku*

We made XIS0 + XIS3 light curves from the source and background regions in the 0.5–10 keV band. Figure 7a

[5] Swift XRT thread:http://www.swift.ac.uk/analysis/xrt/digest_cal.php

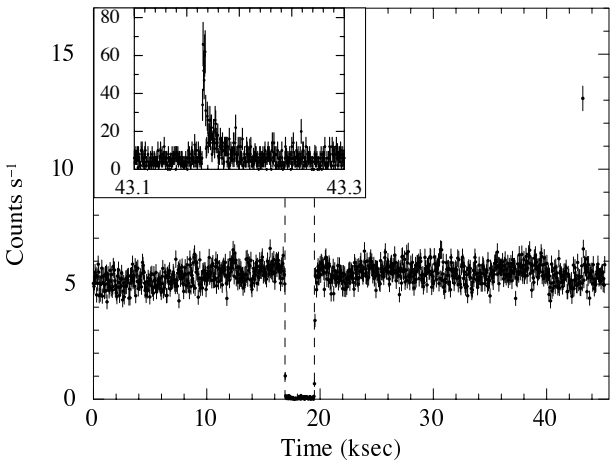

Fig. 6. Light curve obtained with the Chandra observation in the 0.5–10 keV band. The bin size is 46 s. The time origin of the plot was MJD 53093.96450. Dashed lines show the predicted time of the ingress and egress of the eclipse based on in't Zand et al. (2003). Top-left panel shows the zoomed up light curve around the burst.

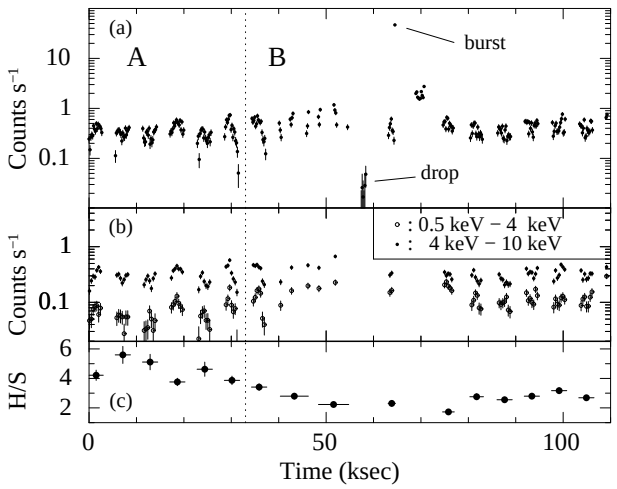

Fig. 7. (a) Suzaku light curve of XIS0+3 in the 0.5–10 keV band. The bin size is 192 s. The time origin is MJD 55090.30904. (b) Light curves of the XIS0+3 in the 0.5–4 keV band (open circles) and 4–10keV band (filled circles). The bin size is 384 s. The intervals of the drop and burst were removed from the plot. (c) Hardness ratio of these energy bands. Each bin has approximately 1500 photons in the 0.5–10 keV band. We divided the exposure time into two intervals A and B with the dotted line.

shows the background-subtracted light curve where the bin size is 192 s. The origin of the light curve is MJD 55090.30904 in TBD. We can see fluctuations of the count rate in the light curve. Also a remarkable drop and a burst were seen at around ~ 57 ks and ~ 64 ks, respectively. The burst lasted for a few hours. The detailed analysis and discussion on the burst is reported in Iwai et al. (2014).

During the drop, the combined count rate of XIS0 + 3 was 0.025 ± 0.026 cts s^{-1}. We could not observe the start and end of the drop due to the Earth occultation or the SAA passage. The upper and lower limits for the duration of the drop were 8296 s and 1368 s, respectively. Some dips are reported in in't Zand et al. (2003). However, the duration of the dipping activity was ~ 50 s, which is quite shorter than that of the drop observed with Suzaku. The averaged count rate excluding the burst and drop was 0.425 ± 0.005 cts s^{-1}.

During the Suzaku observation, two eclipses were predicted, from MJD 55090.73879 to 55090.76884 and from 55091.25377 to 55091.28382. The expected times of the ingresses and egresses are shown with dashed lines in the zoomed up light curve (figure 8). Arrows in the figure show the predicted intervals of the eclipses. Due to both the Earth occultation and the SAA passage, only the first 288 s and 1464 s of the predicted intervals were observed. In contrast to the previous researches and our Chandra result in section 3.2.1, no large decrease in the count rate was seen during the both predicted eclipses. The count rates were 0.14 ± 0.04 cts s^{-1} in the first predicted eclipse and 0.30 ± 0.03 cts s^{-1} in the second one. On the other hand, the count rate in an interval of 288 s just before the first ingress was 0.25 ± 0.06 cts s^{-1}, and that of 1464 s just before the second ingress was 0.45 ± 0.03 cts s^{-1}. The count rates during the predicted eclipses are thus lower than the count rates before the eclipses. The low count rates might suggest that weak eclipses were observed. However, the average duration of the transition for ingress was 27.3 ± 0.8 s, and the mid point of the transition occurred within +1.8 s/−2.5 s from the predicted time (in't Zand et al. 2003). The prediction about the time of the transition mid point could be affected by the change of the orbital period and the uncertainty of the orbital period. The upper limit of $\dot{P}/P$ was estimated to be 1×10^{-16} s^{-1} at MJD 52066.259477 (in't Zand et al. 2003). GRS 1747-312 had completed 5873 revolutions since then, and the change of the orbital period could affect the predicted times of the mid points by 3.4 s at most. The uncertainty of the orbital preiod is 7×10^{-9} d $= 6 \times 10^{-4}$ s (in't Zand et al. 2003). After the 5873 revolutions, the accumulation of the uncertainty could change the predicted time of the mid points by 3.6s at most. Thus the mid point of the transition should be coincident with the prediction within +8.8 s/−9.5 s. The Suzaku light curve does not show these characteristics clearly. Note that the count rate during the Suzaku observation was highly fluctuated. Figure 9 shows a histogram of the count rate excluding the burst, drop, and the durations of the predicted eclipses. The count rate sometimes became lower than that during the interval of the eclipses. Thus the low count rates during the predicted eclipses can be explained by the fluctuation, though the weak eclipse cannot be fully rejected.

Figure 7b shows the background subtracted light curves in the 0.5–4 keV and 4–10 keV bands. The bin size is 384 s. Figure 7c shows the hardness ratio given by H/S, where H and S represent the count rates in the 4–10 keV and 0.5–4 keV band, respectively. The bin size was adjusted so that ~ 1500 photons in the 0.5–10 keV band were included in each bin. During the first ~ 30 ks of

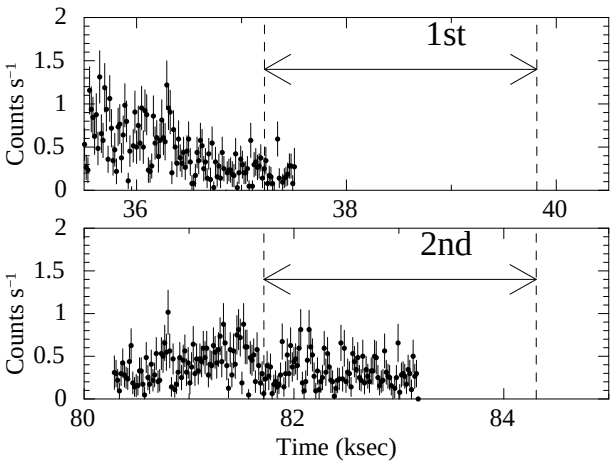

Fig. 8. Zoomed-up light curves in the 0.5–10keV band around the predicted eclipses during the Suzaku observation. The time origin is MJD 55090.30802 and the bin size is 16 s. The dashed lines show the predicted time of the ingress and egress of the eclipses. The arrows indicate the intervals of the predicted eclipses.

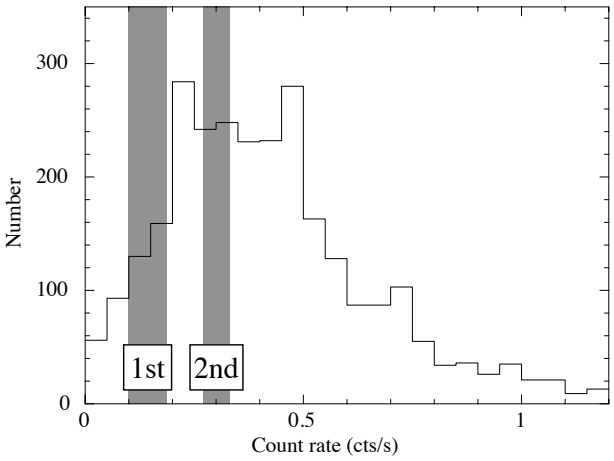

Fig. 9. Histogram of the count rate in the 0.5–10keV band during the Suzaku observation, excluding the burst and drop, and the duration of the predicted eclipses. To make the histogram, we used the count rates binned with 16 s. The gray areas indicate the range of the count rates during the predicted eclipses.

the observation, the count rate in the 0.5–4 keV band was small with < 0.1 cts s^{-1}. The count rate then increased to $\gtrsim 0.1$ cts s^{-1}. On the other hand, the count rate in the 4–10 keV band was relatively stable. As a result, the hardness ratio decreased.

We divided the observation time into two intervals, designated as A and B, with the dotted line in figure 7. The time of the drop and the burst was removed from interval B. During interval A, the hardness ratio generally exceeded 4, while the hardness ratio decreased and then kept constant at ~ 3 during interval B.

3.2.4. Swift

Figure 10 shows the background-subtracted light curves in the 0.5–10 keV band of each observation. The curves are plotted in TDB and binned with 15 s. The time origins of these curves are MJD 56369.87667 and 56375.09391, respectively.

During the 1st observation, the light curve had no remarkable structure. The averaged count rate was 1.85 ± 0.07 cts s^{-1}. During the 2nd observation, on the other hand, a sudden decrease in the count rate was seen at ~ 500 s. The 2nd observation covered the time of the predicted ingress of the eclipse at MJD 56375.09967 (in't Zand et al. 2003), which is shown with the dashed line in figure 10. Thus the sudden decrease was coincident with the expected time of the ingress. Averaged count rates before and after the decrease were 1.8 ± 0.1 cts s^{-1} and 0.10 ± 0.03 cts s^{-1}, respectively.

3.3. Spectrum

3.3.1. Chandra

We investigated the spectrum outside the eclipse to know the properties during the outburst. We extracted the ACIS spectra from the source and background regions. Figure 11 (a) shows the background subtracted spectrum in the 0.5–10 keV band. We binned the spectrum so as to contain at least 10 photons in each bin.

In the spectrum, no clear line-like features were seen. Then we tried to describe the spectrum with an absorbed power-law model, where the "phabs" model in the spectral fitting package `XSPEC` (Arnaud 1996) was used for the absorption model. This model adopts the cross sections of Balucinska-Church & McCammon (1992) with the solar abundance of Anders & Grevesse (1989). The result of the fitting was not acceptable with $\chi^2/\nu = 1.49$ ($\nu = 634$). Figure 11 (b) shows the residuals between the data and the best-fitted single power-law model. There are large residuals below ~ 3 keV. Neither a blackbody model ($\chi^2/\nu = 8.26$) nor a disk blackbody model (Mitsuda et al. 1984; Makishima et al. 1986) ($\chi^2/\nu = 2.47$) can describe the spectrum.

Then we examined several two-components models which are usually used to represent spectra of LMXBs. First, we attempted to fit the data with a model which consists of a disk blackbody component and a blackbody component from the surface of the neutron star. The result of the fitting was not acceptable with $\chi^2/\nu = 1.25$ ($\nu = 632$). Second, we tried a model consisting of a disk blackbody and a Comptonized emission, assuming that only the photons from the surface of the neutron star are Comptonized. We used the "CompTT" model in `XSPEC` (Titarchuk 1994) to describe the Comptonized emission. In this Comptonization model, a spherical distribution was assumed for the Comptonizing hot plasma. This model was not rejected with $\chi^2/\nu = 1.15$ ($\nu = 630$). The best-fit parameters were the following: the absorption column density $N_{\rm H} = 1.13 \pm 0.06 \times 10^{-22}$ cm^{-2}, the temperature at the inner disk radius $kT_{\rm in} = 1.0^{+0.2}_{-0.1}$ keV, the temperature of the seed photons for the Comptonization $kT_{\rm seed} = 0.61^{+0.04}_{-0.03}$ keV, the temperature of the electrons for the Comptonization $kT_e = 8^{+7}_{-2}$ keV, and the plasma optical depth $\tau = 12 \pm 2$. Then we tested a "blackbody + CompTT" model, in which only the photons from

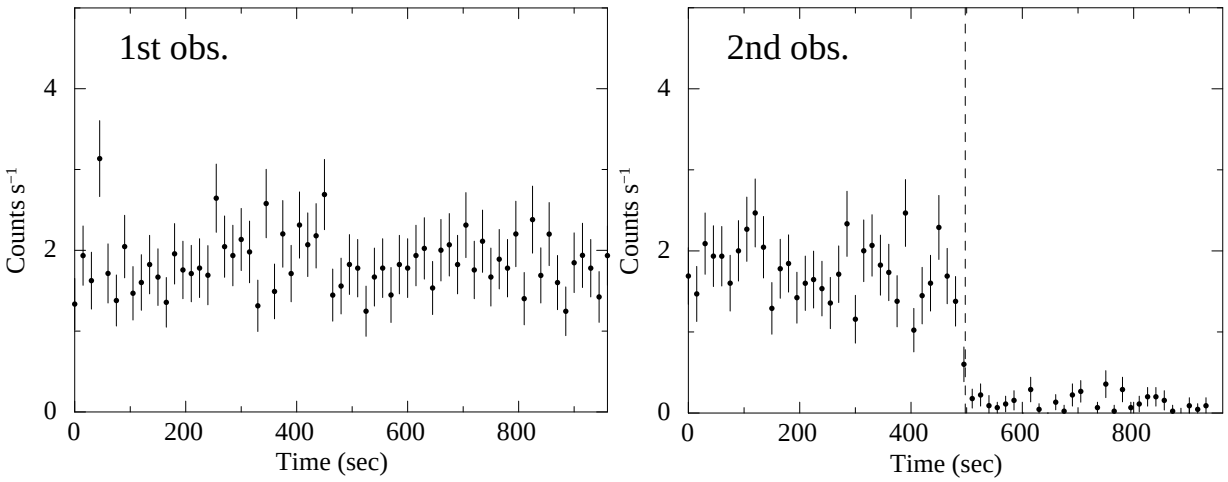

Fig. 10. Swift light curves in the 0.5–10 keV band during the 1st observation (left) and the 2nd observation (right). The bin size is 15 s. The time origins are MJD 56369.87667 and 56375.09391, respectively. The dashed line in the right panel shows the predicted time of the ingress of the eclipse.

the accretion disk are Comptonized. Since the electron temperature for the Comptonization was not sensitive in the fitting, we fixed the value to that in the previous work, $kT_{\rm e} = 5.4$ keV (in't Zand et al. 2000). This model was also not rejected with $\chi^2/\nu = 1.11$ ($\nu = 631$). The best-fit parameters are summarized in table 3. We also checked the model that both of the surface of the neutron star and the accretion disk supply seed photons to the same Comptonizing hot plasma. Since this model was also not sensitive to the electron temperature, we fixed $kT_{\rm e}$ to 5.4 keV. The model was not rejected with $\chi^2/\nu = 1.18$ ($\nu = 630$). We obtained the best-fit parameters as $N_{\rm H} = 0.94 \pm 0.03 \times 10^{-22}$ cm^{-2}, $kT_{\rm seed}$(disk) = $0.69^{+0.02}_{-0.03}$ keV, $kT_{\rm seed}$(neutron star) = $2.28^{+0.09}_{-0.06}$ keV and $\tau < 1.2$. Thus the last three models cannot be distinguished in terms of the statistics. Since the "blackbody + CompTT" model was applied for the GRS 1747−312 spectrum obtained with BeppoSAX in the 0.5–100 keV band in in't Zand et al. (2000), we mainly investigate the model hereafter. Figures 11 (a) and (c) show the best-fit model and the residuals between the data and model, respectively. The absorption column density of $N_{\rm H} = (0.99 \pm 0.03) \times 10^{22}$ cm^{-2} was slightly lower than that for Terzan 6, $N_{\rm H} = (1.2 \pm 0.1) \times 10^{22}$ cm^{-2}, which was estimated via interstellar reddening (Barbuy et al. 1997; Predehl & Schmitt 1995).

Next we studied a spectrum during the eclipse (figure 12). The spectrum was binned so that each bin has at least 10 photons. We tried to fit the spectrum with an absorbed CompTT model. Similar to the fitting for the spectrum outside the eclipse, the electron temperature of the CompTT model was fixed to 5.4 keV. The absorption was also fixed to the value outside the eclipse, $N_{\rm H} = 0.99 \times 10^{22}$ cm^{-2}. The fitting was acceptable with $\chi^2/\nu = 0.78$ ($\nu = 15$). The best-fit model and residuals are shown in figure 12, and the best-fit parameters are summarized in table 3. There were no significant changes in the CompTT parameters, except for the normalization,

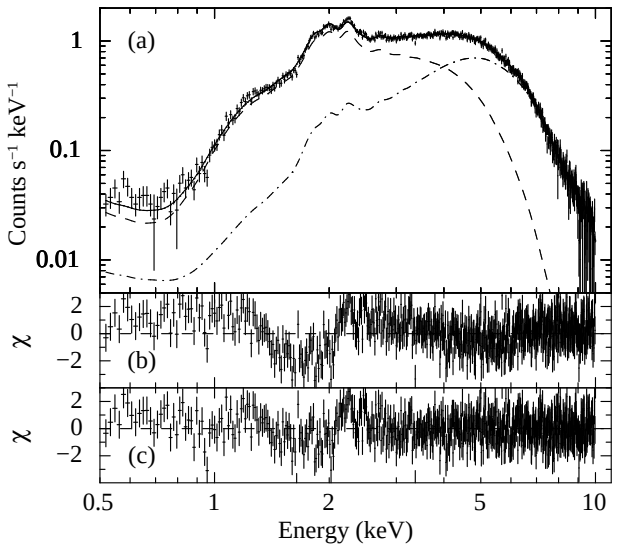

Fig. 11. (a) ACIS spectrum outside the eclipse with the best-fit blackbody (dashed) + CompTT (dash-dotted) model. (b) Residuals between the data and the best-fit single power-law model. (c) Residuals between the data and the blackbody + CompTT model.

from those obtained with the spectrum of the outside of the eclipse. However, due to its low photon statistics, single component models such as a blackbody or power-law could also describe the spectrum. The flux declined by a factor of $(1.0 \pm 0.2) \times 10^{-2}$ compared to the flux outside the eclipse.

3.3.2. XMM-Newton

Figure 13(a) shows the spectra in the 0.5–10 keV band. The black, red and green data points show the spectra obtained with pn, MOS1 and MOS2, respectively. The bin size of the spectra was set so that each bin contains at least 15 photons.

We tried to fit the spectra with an absorbed power-

Table 3. Best-fit parameters for the Chandra ACIS spectrum.

Interval	Outside eclipse	During eclipse
$N_{\rm H}{}^{*}$	$0.99^{+0.03}_{-0.03}$	0.99 (fixed)
$kT_{\rm BB}$ (keV)	$0.76^{+0.04}_{-0.06}$	-
$R_{\rm BB}$ (km)§	$8.1^{+0.4}_{-0.9}$	-
$F_{\rm BB}{}^{\dagger}$	1.82×10^{-10}	-
$kT_{\rm seed}$ (keV)	$1.8^{+1.1}_{-0.7}$	$1.8^{+0.5}_{-0.2}$
$kT_{\rm e}$ (keV)	5.4 (fixed)	5.4 (fixed)
τ	<15	16^{+8}_{-5}
$F_{\rm CompTT}{}^{\dagger}$	3.87×10^{-10}	5.5×10^{-12}
χ^2/ν (ν)	1.11 (631)	0.78 (15)

* Hydrogen column density in units of 10^{22} cm^{-2}.
§ Radius of the blackbody sphere.
† Observed flux in the 0.5–10 keV band in the unit of erg cm^{-2} s^{-1}.

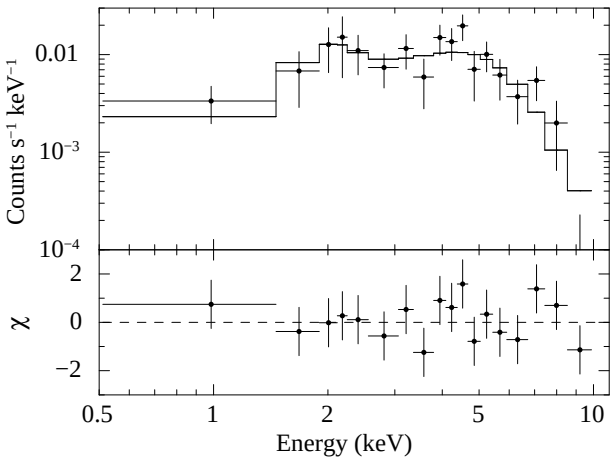

Fig. 12. ACIS-S spectrum during the eclipse fitted with an absorbed CompTT model in the 0.5–10 keV band. Residuals between the data and the best-fit model are shown in the lower panel.

law model. However, the fit was not acceptable with $\chi^2/\nu=1.57$ ($\nu=67$) due to large residuals above $\sim$ 2 keV as shown in figure 13 (b). We then tried the blackbody plus CompTT model as in the case of the analysis of the Chandra spectrum. The electron temperature of the CompTT model was fixed to 5.4 keV. Since the temperature of the seed photons was also insensitive in the fitting we fixed the value to 1.8 keV, which is obtained in the analysis of the Chandra spectrum. The fitting was acceptable with $\chi^2/\nu=1.38$ ($\nu=64$), and the best-fit parameters are summarized in table 4.

3.3.3. Suzaku

XIS spectra of intervals A and B were extracted from the source and background regions, and the spectra were binned so that each bin has at least 20 photons. The XIS1 spectra of intervals A and B after the background subtraction are shown in the upper panel of figure 14 while the lower panel shows the ratio between the both spectra. The X-ray count rates below 4 keV of interval B was found to be higher than that of interval A .

First, the spectrum of interval A was analyzed. The

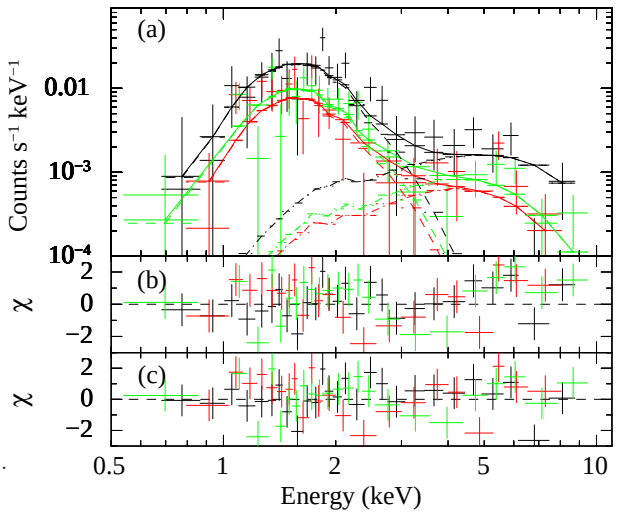

Fig. 13. (a) XMM-Newton spectra obtained with pn (black), MOS1 (red) and MOS2 (green), with the best–fit blackbody (dashed) + Comptonization (dash-dotted) model. (b) Residuals between the data and the best–fit power-law model. (c) Residuals between the data and the best-fit blackbody + Comptonization model.

Table 4. Best-fit parameters for the XMM-Newton spectra.

Parameter	Best-fit value
$N_{\rm H}{}^{*}$	$1.4^{+0.9}_{-0.6}$
$kT_{\rm BB}$ (keV)	$0.33^{+0.09}_{-0.07}$
$R_{\rm BB}$ (km)§	$1.4^{+1.1}_{-0.4}$
$F_{\rm BB}{}^{\dagger}$	6.7×10^{-14}
$kT_{\rm seed}$ (keV)	1.8 (fixed)
$kT_{\rm e}$ (keV)	5.4 (fixed)
τ	<38
$F_{\rm CompTT}{}^{\dagger}$	1.45×10^{-13}
χ^2/ν (ν)	1.37 (65)

* Hydrogen column density in units of 10^{22} cm^{-2}.
§ Radius of the blackbody sphere.
† Observed flux in the 0.5–10 keV band in the unit of erg cm^{-2} s^{-1}.

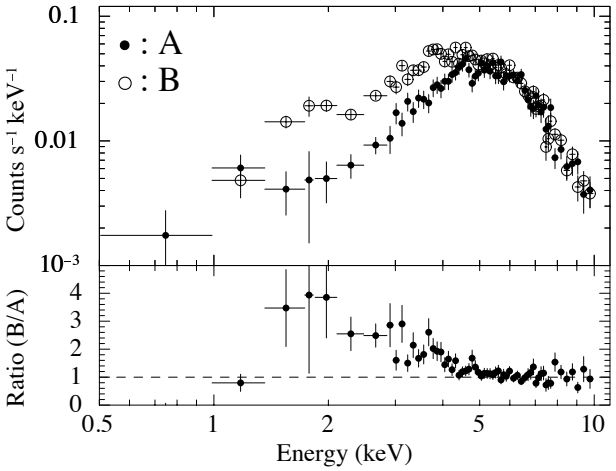

Fig. 14. (Upper panel) Suzaku XIS1 spectra of intervals A (closed circles) and B (open circles). (Lower panel) Ratio between the spectra of intervals A and B.

Table 5. Best-fit parameters of the blackbody + CompTT model fitted to the Suzaku spectra.

	Independent fit		Simultaneous fit	
Interval	A	B	A	B
$N_{\rm H,BB}{}^{*}$	1.2 (fixed)	$1.7^{+1.0}_{-0.9}$	1.2 (fixed)	$1.8^{+0.5}_{-0.4}$
kT (keV)	$0.4^{+0.3}_{-0.1}$	$0.5^{+1.6}_{-0.2}$	$0.4^{+0.1}_{-0.1}$	$1.1^{+0.1}_{-0.1}$
$R_{\rm BB}$ (km)§	$1.2^{+0.4}_{-0.2}$	$1.2^{+0.6}_{-0.2}$	$1.3^{+0.3}_{-0.2}$	$0.40^{+0.02}_{-0.02}$
$F_{\rm BB}{}^{\dagger}$	8.1×10^{-14}	3.57×10^{-13}	7.86×10^{-14}	1.86×10^{-12}
$N_{\rm H,CompTT}{}^{*}$	10^{+4}_{-2}	12^{+2}_{-2}	11^{+3}_{-2}	
$kT_{\rm seed}$ (keV)	<1.9	<1.4	$1.1^{+0.3}_{-0.3}$	
$kT_{\rm e}$ (keV)	5.4 (fixed)	5.4 (fixed)	5.4 (fixed)	
τ	11^{+3}_{-6}	$10.9^{+0.7}_{-0.6}$	12^{+2}_{-2}	
$F_{\rm CompTT}{}^{\dagger}$	0.99×10^{-11}	1.11×10^{-11}	0.97×10^{-11}	
χ^2/ν (ν)	0.91 (185)	1.13 (240)	1.06 (429)	

* Hydrogen column density in units of 10^{22} cm^{-2}.
§ Radius of the blackbody sphere.
† Observed flux in the 0.5–10 keV band in units of erg cm^{-2} s^{-1}. The fluxes of the XIS0 1 and 3 were averaged.

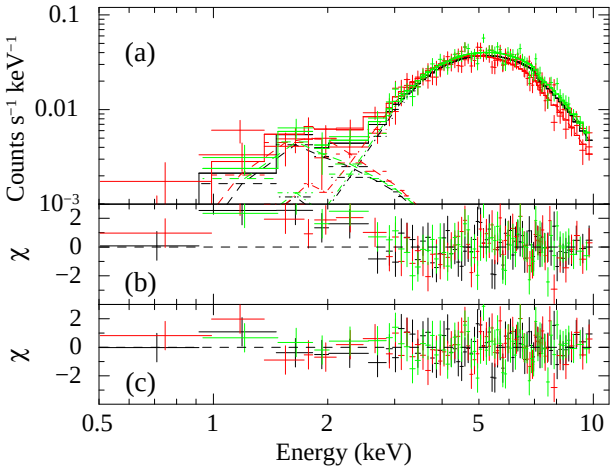

Fig. 15. (a) Suzaku spectra of interval A. The background–subtracted spectra obtained with XIS0, 1, and 3 are represented by black, red and green, respectively. The best–fit blackbody (dashed) + CompTT (dash-dotted) model is also shown, where the column densities for the two components are different (see the text). (b) Residuals between the data and the best-fit single CompTT model. (c) Residuals between the data and the blackbody + CompTT model.

spectra of XIS0, 1 and 3 were simultaneously fitted with an absorbed CompTT model. Here we introduced constant factors, by which the normalization of each sensor was multiplied, to mitigate the uncertainties of the XIS calibration. The fit was not acceptable with $\chi^2/\nu = 1.26$ ($\nu = 187$). Significant residuals below 2 keV can be seen in figure 15 (b). The existence of a soft component is shown by the Suzaku spectra as well as the Chandra and XMM-Newton spectra.

Then we tried to fit the Suzaku spectra with the blackbody + CompTT model. We assumed that the electron temperature of the Comptonization is 5.4 keV as in the case of the Chandra and XMM-Newton spectra. If we assumed the same absorption for the two components, the fit was acceptable with $\chi^2/\nu = 0.98$ ($\nu = 185$). The best-fit parameters of the blackbody component were $kT = 0.07^{+0.02}_{-0.01}$ keV, $N_{\rm H} = 7.1^{+1.4}_{-1.1}\times10^{22}$ cm^{-2}. However, the lower limit of the bolometric luminosity of the blackbody component was 1.0×10^{39} erg s^{-1}, which is significantly larger than the Eddington luminosity for a $1.4M_{\odot}$ neutron star, $\sim 3\times10^{38}$ erg s^{-1}.

The model was then modified so that each component suffers different absorption, given by "phabs1 × blackbody + phabs2 × CompTT". We fixed the column density for the blackbody component to the Galactic value $N_{\rm H,BB} = 1.2\times10^{22}$ cm^{-2}, since if we set the absorption to be free, only an upper limit was obtained. This model can describe the spectrum with $\chi^2/\nu = 0.91$ ($\nu = 185$). The results of the fitting are summarized in figures 15 (a) and (c) and table 5.

Secondly, the spectrum of interval B was analyzed. The spectrum also could not be fitted with a single-component model such as a blackbody or a CompTT model. Thus we tried the absorbed blackbody + CompTT model where the column densities for the two components were different as in the case of interval A. The spectrum of interval B was well described with this model with $\chi^2/\nu = 1.13$ ($\nu = 241$). The results of the fitting are summarized in figure 16 and table 5. Similar to interval A, the CompTT component was strongly absorbed with a column density of $\sim 10^{23}$ cm^{-2}.

Finally, we simultaneously fitted the spectra of intervals A and B with the blackbody + CompTT model. The fact that both spectra are quite similar to each other above $\sim$ 5 keV (figure 14) suggests that both spectrum can be explained by the same CompTT model, but they require a different blackbody component. In this case, the fit was acceptable with $\chi^2/\nu = 1.06$ ($\nu = 420$). The best-fit parameters are summarized in table 5.

The absorption column density of $N_{\rm H} \sim 10^{23}$ cm^{-2} was much higher than the value obtained from the spectrum during the Type-I burst, 1.46×10^{22} cm^{-2} (Iwai et al. 2014). Thus we investigated the lower limits of the column density for several spectral models. When we fitted the spectrum of interval A with the "blackbody + CompTT" model with a free kT_e value, a lower limit of the absorption

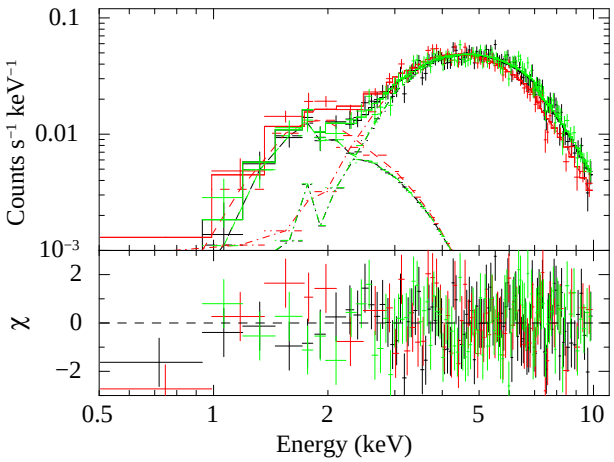

Fig. 16. Suzaku spectra of interval B. The best-fit blackbody + CompTT model is also shown. The definitions of the colors and lines are the same as those in figure 15. Residuals between the data and the best-fit model are shown in the lower panel.

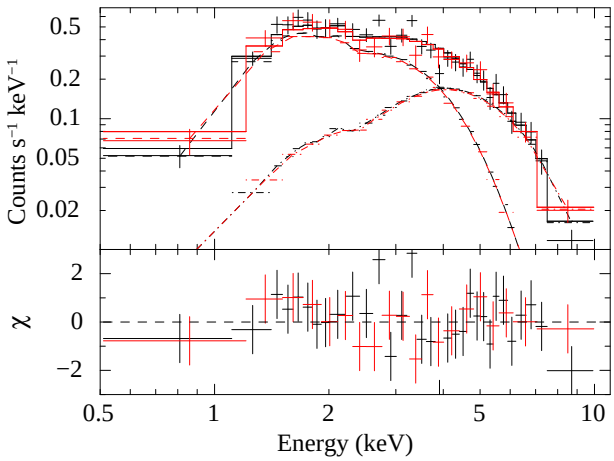

Fig. 17. Swift XRT spectra outside the eclipse. Black and red represent the 1st and 2nd observations, respectively. The best-fit blackbody (dashed) + CompTT (dash–dotted) model is also shown. Residuals between the data and the best-fit model are shown in the lower panel.

column density of 7.6×10^{22} cm^{-2} was obtained when $kT_{\rm e}$ was 2.4 keV. We also tested the spectrum model of "blackbody + blackbody", then we obtained the lower limit of $N_{\rm H} = 7.8 \times 10^{22}$ cm^{-2}. Thus we concluded that the absorption column density during the Suzaku observation was significantly higher than the interstellar absorption, independent on the spectral fitting models.

We also investigated the HXD PIN spectrum, but the spectrum turned out to be significantly contaminated by another bright source as described in appendix. Thus the HXD data are not used in this paper.

3.3.4. Swift

The XRT spectra of the 1st and 2nd observations outside the eclipse are shown in figure 17. To obtain the spectrum of the 2nd observation, only the data until 30 s before the predicted ingress were used. The shapes of the two spectra are quite similar to each other, and we simultaneously analyzed the spectra to increase the photon statistics.

We tried to describe the spectra with the blackbody + CompTT model. All parameters except for the normalizations were fixed to the values obtained from the Chandra analysis (table 3). The ratio between the normalizations of blackbody and of CompTT was fixed to the value of the Chandra result. The fit was acceptable with $\chi^2/\nu = 1.11$ ($\nu = 50$). The observed flux was decreased from the Chandra flux by a factor of 0.86 ± 0.04 for the 1st observation and 0.69 ± 0.04 for the 2nd observation.

The spectrum during the eclipse has too low statistics to be studied in detail. If we applied the same model as that fitted to the spectrum outside the eclipse, the flux in the 0.5–10 keV band was $(5.1 \pm 1.9) \times 10^{-12}$ erg cm^{-2} s^{-1}. This value is lower than that outside the eclipse by a factor of $(1.6 \pm 0.6) \times 10^{-2}$.

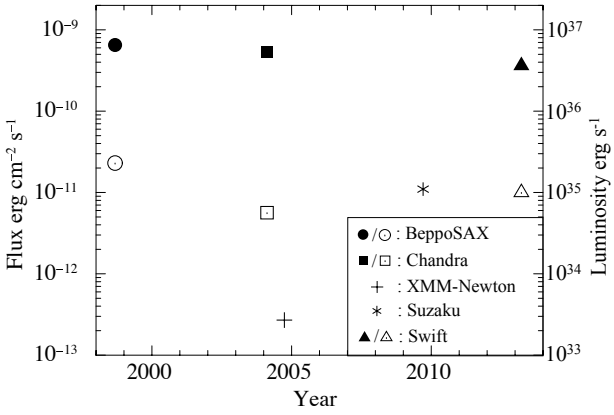

Fig. 18. Observed flux of GRS 1747−312 in the 2.0-10 keV band obtained in several observations, including the previous research (in't Zand et al. 2000). Filled and open marks show the flux outside and during the eclipses, respectively. Vertical axis on the right hand side indicates the luminosity assuming the distance of 9.5 kpc.

4. Discussion

4.1. Long-term variation of the X-ray flux

Figure 18 shows the plot of the observed flux in the 2.0–10 keV band obtained in the Section 3.3. The BeppoSAX result (in't Zand et al. 2000) is also plotted. The flux outside and during the eclipses are shown separately.

We can see that the flux of the outburst phase outside the eclipses is roughly constant at $\sim 5 \times 10^{-10}$ erg cm^{-2} s^{-1}. The flux during the eclipses is also constant at $\sim 10^{-11}$ erg cm^{-2} s^{-1}. Thus the flux during the eclipses is usually ~ 2 % of that outside the eclipses. However, when the XMM-Newton observed, the flux decreased further to 2.7×10^{-13} erg cm^{-2} s^{-1}. GRS 1747−312 thus shows large variability even outside the outburst phase.

4.2. Predicted eclipses and observations

Both of the Chandra and Swift light curves show ingresses at the predicted time, MJD 53094.16016 ($n = 1996$) and MJD 56375.09967 ($n = 8367$), respectively. In the Chandra light curve, an egress was also detected at MJD 53094.19020 ($n = 1996$). Even during these eclipses, X-rays were observed. The ratio of the flux compared to that outside the eclipse was $\sim 2 \times 10^{-2}$. Such flux detected even during eclipses was reported in other eclipsing LMXBs; 2.7 ± 1.0 % for X 1658−298 (Oosterbroek et al. 2001) and 5–10 % for EXO 0748−676 (Bonnet-Bidaud et al. 2001; Homan et al. 2003).

During the Suzaku observation, two eclipses were predicted from MJD 55090.73879 to MJD 55090.76882 ($n = 5873$) and from MJD 55091.25378 to MJD 55051.28380 ($n = 5874$). However, no flux drops were seen during the predicted times as shown with dashed lines in figure 8. One may argue that the time stamped on the Suzaku data was incorrect. We confirmed that the decrease of the XIS count rate of unscreened data exactly synchronized with the SAA passages and Earth occultations which were calculated from the satellite orbit and attitude. We thus verified the time stamped on the XIS data, and the vanishing of the eclipsing event is not an artifact.

Suzaku observed the sudden drop of the flux at around 60 ks in figure 7, just before the type-I burst. One may argue that the orbital phase would have been changed for some reasons and the drop could be the eclipse. However, the Swift observation, which was conducted after the Suzaku observation, confirmed that the eclipse occurred at the predicted time. It is reasonable to consider that the drop of the flux was different from the eclipse event.

Even though the flux did not change at the predicted ingresses, some other properties might change. We then checked the position of Source 1 during the second predicted eclipse around 83 ks in figure 8. The difference of the positions between outside and during the eclipse was $(\Delta\alpha, \Delta\delta) = (+1\farcs4 \pm 1\farcs0, +0\farcs2^{+1\farcs3}_{-1\farcs2})$. On the other hand, the root mean square of the fluctuation of the Suzaku pointing direction during this observation was $8\farcs9$ along the right ascension axis, and $5\farcs0$ along the declination axis. Thus there was no significant deference between the source positions during and outside the eclipse. We also checked the spectrum. Figure 19 shows the XIS1 spectrum obtained during the predicted second eclipse (filled circles) and that after the predicted egress (open circles), which corresponds to 85–90 ks in figure 8. We see no significant change in the spectra. We found that both spectra can be described by the blackbody + CompTT model with the same parameters as those listed in the column of "Independent fit, Interval B" in table 5. Thus neither the Suzaku image nor spectrum showed a change coincident with the predicted eclipse.

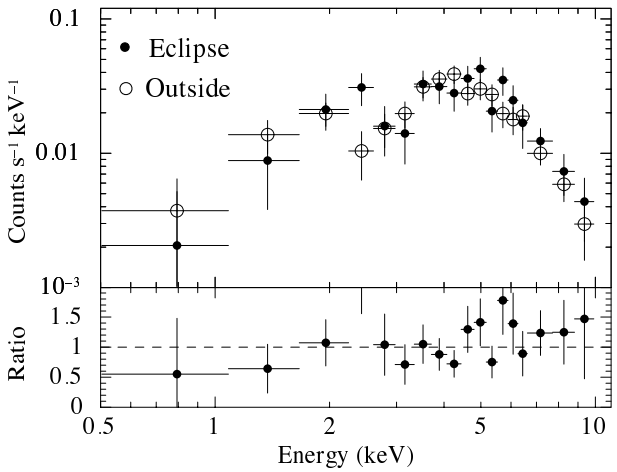

Fig. 19. Suzaku spectra during the predicted second eclipse (filled circles) and after the eclipse (open circles) obtained with XIS1. Ratio of the spectrum outside the eclipse to that during the eclipse is shown in the lower panel.

4.3. Lapse of Eclipse

We should note that the clear eclipsing events have been observed only during the outburst state. One of the possibilities to explain the lapse of the clear eclipse in the Suzaku observation is that there is a contaminant X-ray source quite close to GRS 1747−312. When GRS 1747−312 is not in the outburst state, observed X-rays originate in the contaminant source rather than GRS 1747−312. When GRS 1747−312 is in the outburst state, we can see the eclipse event, and the remaining X-ray flux during the eclipse is due to the contaminant source. This scenario can explain why the X-ray flux during the eclipse is close to that observed with Suzaku (figure 18). Based on the X-ray luminosity function and the radial profile of surface brightness of 47 Tuc (Grindlay et al. 2001; Gebhardt & Fischer 1995), expected number of X-ray source of $> 10^{35}$ erg cm^{-2} s^{-1} within the core radius of a globular cluster is ~ 0.14. Since the core radius of GRS 1747−312 is $3\farcs3$, a contaminant source that cannot be resolved with Suzaku is not so unlikely.

The flux of the contaminant source is mostly around $\sim 10^{-11}$ erg cm^{-2} s^{-1} (figure 18), which corresponds to the luminosity of $\sim 2 \times 10^{35}$ erg s^{-1} assuming the distance of 9.5 kpc. The flux occasionally decreases to a few hundredths of the usual value as suggested by the XMM-Newton observation. If the type-I burst observed with Suzaku (see figure 7; Iwai et al. 2014) came from the contaminant source, the contaminant source should be a neutron star X-ray binary. However, it is also possible that we saw the superposition of the contaminant source and the type-I burst occurred at GRS 1747−312.

If this contaminant scenario is correct, the position of the X-ray source might change during the eclipses. We made the projection profiles of the Chandra image along the declination axis during and outside the eclipse separately. The profiles were fitted with a Gaussian function, and we found no significant changes in the peak position and the width of the Gaussian function. We also examined the Swift image during the eclipse, and the peak position is also consistent with GRS 1747−312 though the statistics are poor (see section 3.1.4). Thus we see no significant

evidence for the contaminant source in our observational data. Note, however, that the Chandra observation analyzed in this paper was conducted with the CC mode and a one-dimensional image was obtained. The other Chandra HRC-I observation did not cover the predicted eclipse (in't Zand et al. 2003). A future Chandra observation covering the eclipse might be able to detect the change of the source position.

The lapse of the eclipse during the Suzaku observation might be explained if direct X-rays from a neutron star and an accretion disk are perfectly blocked by thick material between the companion star and the neutron star (figure 20). In this condition, direct emission from near the neutron star that can be screened by the companion star cannot be seen. Then we see no change of the flux and spectrum at the predicted time of the eclipse. To block the direct X-rays, a column density larger than $N_{\rm H} \geq 10^{24}$ cm^{-2} is required. However, we saw the X-ray flux of $\sim 10^{-11}$ erg cm^{-2} s^{-1} during the Suzaku observation. We think that the outer parts of the thick material may have lower column density and the Compton scattered X-rays by the hot corona can penetrate the material. That is why the hard component of the Suzaku spectrum suffers the heavy absorption of $\sim 10^{23}$ cm^{-2} (table 5). To explain the soft component, we further assume that the outer parts of the material is patchy. Then we tried to fit a partially covered model to the Suzaku spectra. The CompTT model was assumed, and the "pcfabs" model in `XSPEC` was used to represent the partial covering. The model can be written as "phabs1 × pcfabs × CompTT". The "pcfabs" is given by

$$(\text{pcfabs}) = f(\text{phabs2}) + (1 - f), \quad (1)$$

where f represents the covering fraction. The phabs1 was installed to represent the interstellar absorption and was fixed to be 1.2×10^{22} cm^{-2}. The parameters of the CompTT component were assumed to be the same for both intervals A and B. Similar to the previous analyses, the electron temperature was fixed to be 5.4 keV. The fitting was acceptable with $\chi^2/\nu = 1.07$ ($\nu = 426$). The best-fit parameters are summarized in table 6. The absorption column density and covering fraction decreased from interval A to interval B, and this can explain the soft component increased from interval A to interval B.

The partial covering model cannot describe the XMM-Newton spectrum with $\chi^2/\nu = 1.61(\nu = 64)$. Therefore the thick material scenario cannot be adopted to the low-luminosity state generally.

One of the problems of the thick material scenario is that the origin of the thick material is unknown. Furthermore we see no hint of the heavy absorption during the type-I burst at ~ 64 ks (figure 7). The burst had a long duration with photospheric radius expansion, which indicate that the peak luminosity reached the Eddington luminosity (Iwai et al. 2014). Indeed, the bolometric luminosity calculated from the data at the peak was $\sim 3 \times 10^{38}$ erg s^{-1} for 9.5 kpc, which is consistent with the Eddington luminosity for a 1.4 $M_\odot$ neutron star. Thus the direct emission from the neutron star was seen at this moment, definitely. The thick absorber may be photo-ionized during the Type-I burst because of its high luminosity. Then the absorption column density can be less than that during the persistent state. However, we found no evidences for such ionization.

Table 6. Best-fit parameters of the partially covered CompTT model fitted to the Suzaku spectra.

Interval	A	B
$N_{\rm H,pc}$* (10^{22} cm^{-2})	$16.1^{+0.5}_{-0.5}$	$10.5^{+0.3}_{-0.3}$
Covering fraction	$0.970^{+0.007}_{-0.022}$	$0.924^{+0.006}_{-0.006}$
$kT_{\rm seed}$ (keV)	$0.44^{+0.05}_{-0.05}$	
$kT_{\rm e}$ (keV)	5.4 (fixed)	
τ	$11.7^{+0.3}_{-0.2}$	
χ^2/ν (ν)	1.07 (431)	

* Hydrogen column density in units of 10^{22} cm^{-2}.

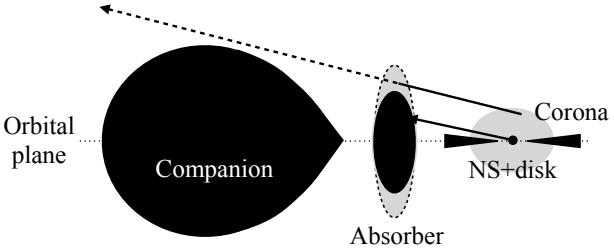

Fig. 20. Schematic view of the thick material scenario to explain the lapse of the eclipse in the Suzaku observation. The direct X-rays from GRS 1747−312 is blocked by thick material between the companion star and the neutron star. Outer parts of the material may be less thick and patchy, and the Compton scattered X-rays can penetrate those parts.

As discussed in section 3.2.3, it cannot be fully rejected that weak eclipsing events were observed during the Suzaku observation. If there was an X-ray corona of which scale height is larger than the companion star, the X-rays are not completely blocked by the companion star even during the interval of the eclipse. In this case, we could see a part of the corona emission even in the eclipse, and we would expect a weak eclipsing event. However, when we assume such a highly extended corona, the steep drop of the flux during the Suzaku observation is hard to be explained.

5. Summary

GRS 1747−312 was observed by Chandra in 2004, XMM-Newton in 2004, Suzaku in 2009 and Swift in 2013. The Chandra and Swift observations were done during the outburst. These observations covered the predicted time of the eclipse, except for the XMM-Newton. This is the first time to study the property of GRS 1747−312 outside the outburst state.

During the Chandra and Swift observations, the eclipses were observed at the predicted time. Remaining X-rays were detected during the eclipses. An averaged 2–10 keV flux outside the eclipse observed with Chandra

and Swift was $\sim 5 \times 10^{-10}$ erg cm^{-2} s^{-1}, but it decreased to $\sim 10^{-11}$ erg cm^{-2} s^{-1} during the eclipse. This feature was consistent with the previous research (in't Zand et al. 2000) and some other eclipsing LMXBs. During the Suzaku observation, on the other hand, the eclipse was not observed. An averaged 2–10 keV flux observed with Suzaku was $\sim 10^{-11}$ erg cm^{-2} s^{-1}, which was comparable to the flux during the eclipse. The XMM-Newton flux was very low at 2.7×10^{-13} erg cm^{-2} s^{-1}.

These results may suggest that another source is located quite close to GRS 1747−312. When GRS 1747−312 is not in the outburst state, the observed X-rays came from the contaminant source rather than from GRS 1747−312. However, we did not obtain clear evidence for the contaminant source in our data.

The results might be explained by thick material ($N > 10^{24}$ cm^{-2}) between the neutron star and the companion star which completely blocked the direct X-rays from the neutron star. Outer parts of the thick material is less thick and patchy, and X-rays Compton scattered by hot corona can penetrate those parts. In fact, the Suzaku spectrum can be described by the partially covered CompTT model. The origin of the thick material, however, is not clear.

Acknowledgments

We thank all the Suzaku team members for their supports. HM is supported by a Grants-in-Aid for Scientific Research from the MEXT, No. 15K13464, 24340039, and 15H02070.

We also wish to acknowledge Dr. Kazunori Ishibashi (Nagoya University) for his helpful comments and suggestions.

Appendix. Suzaku HXD spectrum

The PIN count rate was 0.65 cts s^{-1} in the 15–70 keV band after the subtraction of the Non X-ray Background. The count rate of the Cosmic X-ray Background (CXB) was negligible. On the other hand, the PIN count rate estimated from the XIS count rate and spectrum of GRS 1747−312 was $\sim$ 0.03 cts s^{-1}. The observed PIN count rate was thus $\sim$ 20 times larger. This suggests contamination by other objects.

We searched other X-ray sources near GRS 1747−312 with the SIMBAD database[6]. In the database, there is an X-ray source, IGR J17511−3057 at $(\alpha, \delta)_{\rm J2000.0} = (267.^\circ7861, -30.^\circ9614)$ (Nowak et al. 2009). The position is 19.′4 north from the center of the field of view of the PIN. IGR J17511−3057 exhibited an outburst on 2009 September 11 (Baldovin et al. 2009; Markwardt et al. 2009), which was five days before the Suzaku observation. The count rate on September 16 of IGR J17511−3057 observed with RXTE was ~ 70 counts s^{-1} per a detector (Proportional Counter Unit; PCU) in the 2–25 keV band (Riggio et al. 2011). Assuming a power-law spectrum with $\Gamma = 2.0$, the count rate corresponds to $\sim$ 0.52 cts s^{-1} of PIN. We thus concluded that the PIN count rate was dominated by IGR J17511−3057, and we decided not to use the PIN data for our analysis.

[6] http://simbad.u-strasbg.fr/simbad/

References

Anders, E., & Grevesse, N. 1989, Geochim. Cosmochim. Acta, 53, 197
Arnaud, K. A. 1996, Astronomical Data Analysis Software and Systems V, 101, 17
Aschenbach, B., Briel, U. G., Haberl, F., et al. 2000, Proc. SPIE, 4012, 731
Baldovin, C., Kuulkers, E., Ferrigno, C., et al. 2009, The Astronomer's Telegram, 2196, 1
Balucinska-Church, M., & McCammon, D. 1992, ApJ, 400, 699
Barbuy, B., Ortolani, S., & Bica, E. 1997, A&AS, 122, 483
Bonnet-Bidaud, J. M., Haberl, F., Ferrando, P., Bennie, P. J., & Kendziorra, E. 2001, A&A, 365, L282
Brinkman, A. C., Gunsing, C. J. T., Kaastra, J. S., et al. 2000, ApJL, 530, L111
Canizares, C. R., Davis, J. E., Dewey, D., et al. 2005, PASP, 117, 1144
Chenevez, J., Bozzo, E., Bordas, P., et al. 2013, The Astronomer's Telegram, 4883, 1
Davis, J. E., Bautz, M. W., Dewey, D., et al. 2012, Proc. SPIE, 8443, 84431A
Gebhardt, K., & Fischer, P. 1995, AJ, 109, 209
Garmire, G. P., Bautz, M. W., Ford, P. G., Nousek, J. A., & Ricker, G. R., Jr. 2003, Proc. SPIE, 4851, 28
Gehrels, N., Chincarini, G., Giommi, P., et al. 2004, ApJ, 611, 1005
Grindlay, J. E., Heinke, C., Edmonds, P. D., & Murray, S. S. 2001, Science, 292, 2290
Homan, J., Wijnands, R., & van den Berg, M. 2003, A&A, 412, 799
in't Zand, J. J. M., Bazzano, A., Cocchi, M., et al. 2000, A&A, 355, 145
in't Zand, J. J. M., Hulleman, F., Markwardt, C. B., et al. 2003, A&A, 406, 233
Ishisaki, Y., Maeda, Y., Fujimoto, R., et al. 2007, PASJ, 59, 113
Iwai, M., Dotani, T., Ozaki, M., et al. 2014, Suzaku-MAXI 2014: Expanding the Frontiers of the X-ray Universe, 158
Jain, C., & Paul, B. 2011, MNRAS, 413, 2
Jansen, F., Lumb, D., Altieri, B., et al. 2001, A&A, 365, L1
Kennea, J. A., & Skinner, G. K. 1996, PASJ, 48, L117
Koyama, K., Tsunemi, H., Dotani, T., et al. 2007, PASJ, 59, 23
Kuulkers, E., den Hartog, P. R., in't Zand, J. J. M., et al. 2003, A&A, 399, 663
Lin, J., Nowak, M. A., & Chakrabarty, D. 2009, ApJ, 706, 1069
Liu, Q. Z., van Paradijs, J., & van den Heuvel, E. P. J. 2007, A&A, 469, 807
Lund, N., Budtz-Jørgensen, C., Westergaard, N. J., et al. 2003, A&A, 411, L231
Maeda, Y., Koyama, K., Sakano, M., Takeshima, T., & Yamauchi, S. 1996, PASJ, 48, 417
Makishima, K., Maejima, Y., Mitsuda, K., et al. 1986, ApJ, 308, 635
Markwardt, C. B., Altamirano, D., Swank, J. H., et al. 2009, The Astronomer's Telegram, 2197, 1

Matsuoka, M., Kawasaki, K., Ueno, S., et al. 2009, PASJ, 61, 999
Mitsuda, K., Inoue, H., Koyama, K., et al. 1984, PASJ, 36, 741
Mitsuda, K., Bautz, M., Inoue, H., et al. 2007, PASJ, 59, 1
Murray, S. S., Austin, G. K., Chappell, J. H., et al. 2000, Proc. SPIE, 4012, 68
Oosterbroek, T., Parmar, A. N., Sidoli, L., in't Zand, J. J. M., & Heise, J. 2001, A&A, 376, 532
Nowak, M. A., Paizis, A., Wilms, J., et al. 2009, The Astronomer's Telegram, 2215, 1
Pavlinsky, M. N., Grebenev, S. A., & Sunyaev, R. A. 1994, ApJ, 425, 110
Predehl, P., Hasinger, G., & Verbunt, F. 1991, A&A, 246, L21
Predehl, P., & Schmitt, J. H. M. M. 1995, A&A, 293, 889
Riggio, A., Papitto, A., Burderi, L., et al. 2011, A&A, 526, A95
Serlemitsos, P. J., Soong, Y., Chan, K.-W., et al. 2007, PASJ, 59, 9
Strüder, L., Briel, U., Dennerl, K., et al. 2001, A&A, 365, L18
Takahashi, T., Abe, K., Endo, M., et al. 2007, PASJ, 59, 35
Titarchuk, L. 1994, ApJ, 434, 570
Turner, M. J. L., Abbey, A., Arnaud, M., et al. 2001, A&A, 365, L27
Uchiyama, Y., Maeda, Y., Ebara, M., et al. 2008, PASJ, 60, 35
Uchiyama, H., Ozawa, M., Matsumoto, H., et al. 2009, PASJ, 61, 9
Weisskopf, M. C., Tananbaum, H. D., Van Speybroeck, L. P., & O'Dell, S. L. 2000, Proc. SPIE, 4012, 2
Weisskopf, M. C., Aldcroft, T. L., Bautz, M., et al. 2003, Experimental Astronomy, 16, 1
Wolff, M. T., Ray, P. S., Wood, K. S., & Hertz, P. L. 2009, ApJS, 183, 156